Erschienen in: The Analyst ; 143 (2018), 17. - S. 4040-4050
https://dx.doi.org/10.1039/c8an00706c

Design concepts in absorbance optical systems for analytical ultracentrifugation

Joseph Pearson, †[a] Marcel Hofstetter,†[b] Thomas Dekorsy,[b,c] Michael Totzeck[d] and Helmut Cölfen*[a]

Analytical ultracentrifugation is a powerful technique for analyzing particles in solution, and has proved valuable for a wide range of applications in chemistry, biochemistry and material sciences for many years. The field is presently seeing a resurgence of instrument development from commercial and academic groups. To date, no modern optical modeling techniques have ever been applied to the basic imaging properties of the optical system in analytical ultracentrifugation. In this manuscript we provide a contextual framework for the application of such techniques, including an overview of the essential optical principles. The existing commercial and open source detection systems are evaluated for imaging performance, highlighting the limitations of chromatic aberration for broadband acquisitions. These results are the inspiration for a new mirror-based design, free of chromatic aberration. Our findings present a path forward for continued development in imaging and detector technology, where improved data quality will now push the limits of detection and resolution of analytical ultracentrifugation for years to come.

1. Introduction

Analytical ultracentrifugation (AUC) is conducted by means of an optical system recording the radial concentration profile of a solution while in a spinning rotor. Many excellent introductions to AUC experimental methods are readily available.[1–3] This manuscript is concerned with the fundamental aspects of AUC instrumentation hardware. Details of AUC instrumentation concerning acquisition timing, light source and detector opto-electronics, and basic overviews of data quality performance have been published previously.[4–7] Here we review the essential optical design principles involved in the beam path construction of absorbance optics for AUC. The architecture of existing absorbance detector optics is evaluated and provides the inspiration for the design of a new mirror based assembly, free of chromatic aberration.

Beckman-Coulter has for decades, and until recently, been the sole industrial provider of AUC instrumentation. Serving the academic and industrial scientific communities with the ProteomeLab, since the early 90s: the base centrifuge platform featuring the most widely used optical system in AUC (the XL-A absorbance detector). The XL-A is a radial scanning lens imaging absorbance detector, with limited possibility for three wavelength spectral scanning experiments. The optical hardware of the XL-A has remained essentially unchanged since its first introduction in 1991, and has never been completely characterized for optical performance. In the last ten years, new hardware has emerged from academia for broadband absorbance imaging, as part of the Open AUC initiative;[8–12] the multiwavelength (MWL) absorbance detector. The MWL detector has been continually developed by several academic groups since its introduction in 2008, and a spin off version has also been commercialized.[11,12] The evolution of MWL detector designs, including the latest advancements, was reviewed recently, also showing the introduction of mirror imaging optics, developed as a result of the design efforts detailed within this manuscript.[5]

We begin by describing the basic optical principles considered in the evaluation and design of optical systems in general, and detail the framework pertinent to AUC absorbance imaging. Next we outline the constraints and optical limits confronted when optimizing detector design.

The software *OpticStudio* available from *Zemax* is used to model and characterize the imaging performance of existing design architectures. To overcome the limitations imposed by the chromatic aberration of lens based imaging optics, a new mirror optics design is conceived. Here we describe the concept for the mirror imaging design and the complete

[a]University of Konstanz, Department of Chemistry, Universitätsstrasse 10, Konstanz 78457, Germany. E-mail: helmut.coelfen@uni-konstanz.de
[b]University of Konstanz, Department of Physics, Universitätsstrasse 10, Konstanz 78457, Germany
[c]Institute for Technical Physics, German Aerospace Center, Pfaffenwaldring 38-40, 70569 Stuttgart, Germany
[d]Corporate Research and Technology, Carl Zeiss AG, Carl-Zeiss-Straße 22, 73447 Oberkochen, Germany
†These authors contributed equally to this article.

optical parameterization and modeling evaluations from which the newest hardware was inspired. Some suggestions for further design improvements are provided in the conclusion.

2. Experimental methods

2.1 Aberration and imaging theory

Optical design modeling and evaluations have been conducted with adherence to the basic definitions and mathematical treatment of aberration and imaging theory.[13] Aberration theory is typically considered in terms of wave or ray aberrations. Within the former description, plane objects in the field of view are imagined as collections of infinitesimal point objects. Each point object is assumed to radiate a spherical wavefront. In the case of perfect image formation, the optical system converts the radiated wavefront into a spherical wavefront emitting from the exit pupil, converging to a perfect point on an image plane. Aberrations inherent to the optical system will result in deformation of the converging wavefront in image space. The optical path difference between the aberrated wavefront and a spherical reference sphere is called wave aberration. The wave aberration of a fixed object point is dependent on the object point's location and the pupil coordinates of the optical system. In the case of rotationally symmetric and centered imaging systems, wave aberration, W, can be expressed in terms of a polynomial power series expansion in polar pupil coordinates (r, φ) and object field height, y, eqn (1);

$$W = b_1 r^2 + b_2 y r \cos\varphi + c_1 r^4 + c_2 y r^3 \cos\varphi + c_3 y^2 r^2 \cos^2\varphi + c_4 y^2 r^2 + c_5 y^3 r \cos\varphi + \ldots \quad (1)$$

with radial pupil coordinate r and the azimuth angle φ, as typically defined in optical systems.[13] Each term in eqn (1) represents well known types of monochromatic aberration, except for the second order terms with the coefficients b_1 and b_2. Terms, b_1 and b_2 are not regarded as aberrations because they describe the defocus and the magnification of the conjugated image point respectively. The terms with coefficients c_i are the so-called monochromatic primary Seidel aberrations (c_1, spherical aberration; c_2, coma; c_3, astigmatism; c_4, field curvature; c_5, distortion).

In the case of polychromatic imaging, chromatic aberrations are induced by the wavelength dependence of the refractive index. Thus, every term in eqn (1) will differ between various wavelengths. The wavelength dependency of the paraxial image position and image height are known as the primary chromatic aberrations, and are referred to as axial and lateral chromatic aberration respectively.

Another description of aberrations is given by means of rays that are perpendicular to the aberrated wavefront. The lateral displacement of a ray's intersection point with the image plane from the ideal reference intersection point is called transverse ray aberration. Wavefront and ray aberrations are related, and may be converted into each other.[14] Common tools in optical design software, such as *OpticStudio* from *Zemax*, for analyzing and identifying aberrations involve plotting the wavefront or transverse ray aberrations over the pupil coordinates of an optical system.

Even in the absence of aberrations, diffraction of light at an aperture affects image formation. The three-dimensional intensity distribution of a single point image is known commonly known as a point spread function (PSF). In the case of an aberration-free optical system with a homogenously illuminated circular aperture, the lateral PSF in the Fraunhofer approximation is represented by the Airy diffraction pattern, eqn (2);

$$I(r') = I_0 \left| \frac{2J_1\left(\frac{2\pi r'}{\lambda}\mathrm{NA}\right)}{\frac{2\pi r'}{\lambda}\mathrm{NA}} \right|^2 \quad (2)$$

where r' is the lateral image coordinate, λ the wavelength, NA the numerical aperture, I_0 the peak intensity of the point image and $J_1(x)$ the first order Bessel function. In the case of incoherent illumination, the resolution limit due to diffraction through a circular aperture is often estimated by the Rayleigh criterion. This criterion predicates, that two point sources can be resolved when they are separated by a distance larger than the Airy radius, which is the first zero point of the Airy diffraction pattern,[13] eqn (3);

$$r_{\mathrm{Airy}} = 0.61\frac{\lambda}{\mathrm{NA}} \quad (3)$$

The circular area on the lateral image plane section centered around the maximum of the Airy intensity distribution with a diameter of $d_{\mathrm{Airy}} = 2r_{\mathrm{Airy}}$ is called the Airy disk.[15]

In the presence of aberrations, the shape of the PSF gets altered from the Airy pattern. Typical effects of aberration on the diffraction-limited PSF are, for example, a decrease of the maximum intensity and broadening and displacement of the intensity distribution. However, a point image that is minimally affected by aberration may be limited only by the Airy pattern characteristic of diffraction. Optical systems are considered as diffraction-limited by the Rayleigh criterion if the peak-to-valley value of the wave aberration is smaller than a quarter wavelength.[15]

Optical design programs trace rays, according to the rules of geometrical optics, through an optical system and visualize their intersection points on the image plane in a so-called spot diagram. A spot diagram approximates the broadening of a point image as a geometrical spot of confusion. In this work, the geometric (GEO) radius of a spot diagram is defined as the distance between the chief ray's intersection point on the image plane and the ray farthest from this reference point. While the GEO radius gives information about the maximum point spread, the RMS spot radius gives a better impression on how the individual rays are spread on the image plane. To determine the RMS spot radius, the sum of the squares of the distance between each ray and the reference point (here chief ray) is calculated, averaged over all rays and, finally, the square

root is taken. Additionally, the Airy disk of a chosen primary wavelength can be plotted on the same spot diagram, and if the RMS spot radius of the same wavelength is smaller than the Airy radius, the optical system's imaging performance can be estimated as diffraction-limited.[16]

2.2 AUC optical principles

For application in AUC, an optical system must foremost have the possibility of differentiating the solute from the solvent. An absorbance-based detector accomplishes this by discrimination of extinction coefficients. The goal for optimization in detector design is to record the highest possible radial resolution, while also maximizing the signal to noise ratio of the acquisition. Furthermore, a detector should be able operate across a large dynamic range, that is, it should be able to capture high concentration and low concentration signals within the same imaging field.[7] The light transmission will follow Beer–Lamberts law, according to solution concentration, extinction coefficient, and path length through the sample column. The imaging optics should therefore capture the 12 mm depth of field typical of AUC sample cells. The MWL devices aim to achieve these across a broad spectral region. A bandwidth typical of MWL AUC hardware, 230–700 nm, is considered within the following evaluations.

A concentration gradient formed during centrifugation is the fundamental feature measured in AUC. The concentration gradient will always, as a result of the optical properties differentiating the solute from the solvent, also exist as a refractive index gradient. Designing an optical system capable of imaging a refractive gradient is one of the basic challenges and imposes limits on the maximum resolution possible.

The hardware necessary for synchronizing the acquisitions with the spinning rotor and the subsequent selection of illumination and detector hardware has been described previously.[5] While the design of imaging optics is in many ways correlated with the effectiveness of source and detector hardware, *i.e.* the signal-to-noise ratio of the data, this manuscript focuses on the optimization of imaging quality as assessed by radial resolution.

One of the last publications detailing optical design principals in AUC dates back to 1974.[17] The basic features of AUC detector designs are described, including the challenge of refractive gradient imaging. Many of the principles discussed are still applicable to modern imaging systems, but the tools of computer aided optical design have never been applied. To utilize these tools, we first define a coordinate system relative to the geometry of the typical AUC sample channel, as illustrated in Fig. 1A. In Cartesian coordinates, Z is the optical axis, Y is the direction in which sedimentation occurs, and X is orthogonal to Y and Z. This coordinate system is different from those defined previously,[17,18] but more in-line with the general convention of modern optical design. It is important to note the common practice in AUC of reference to the top and bottom of the cell, conferring orientation in the x direction, where the meniscus is near the top and the centrifugal field is directed top to bottom. Because the centrifuge rotor

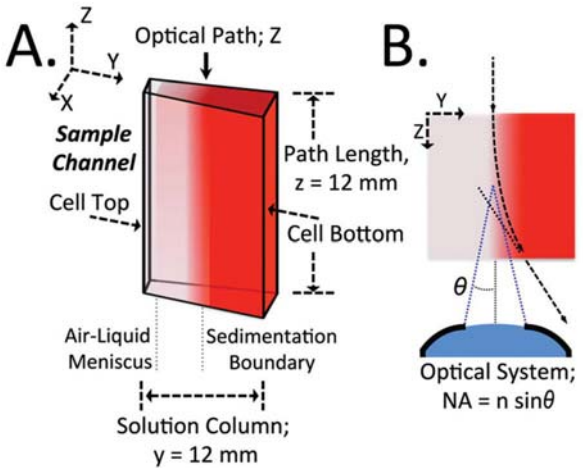

Fig. 1 (A.) Illustration of a typical AUC sample channel, and Cartesian coordinate system definition. (B.) Illustration of the effect of refractive gradient ray bending, *i.e.* refraction, and the relationship to the numerical aperture of the optical system.

spins about a vertical axis, the centrifugal field is perpendicular to earth's gravity. One additional note; it is for conceptual simplicity the Cartesian coordinate system is considered here across the sample channel, whereas in evaluation of experimental AUC data a cylindrical coordinate system is necessary to correctly express the divergence operator in modeling sedimentation behavior.[19]

A typical AUC cell confines a sample between two windows in a sector shaped channel that extends 12 mm in the y dimension and 12 mm in the z dimension. Solute absorption will take place across the entire 12 mm of the z path length, and therefore it is desirable that the imaging optics are able to attain a 12 mm depth of field. The depth of field is usually considered as the maximum interval range of axial displacement of an object point from the position of best focus that leaves the image quality the same. There are many approaches that specific criteria to define the depth of field, δz, mathematically, taking several assumptions into account. In the case of diffraction-limited systems, the depth of field is estimated by, eqn (4);[20]

$$\delta z = \frac{n \cdot \lambda}{\mathrm{NA_{Obj}}^2} \tag{4}$$

here, n is the refractive index in object space and $\mathrm{NA_{Obj}}$ the object space numerical aperture. The $\mathrm{NA_{Obj}}$ is defined by the illumination ray cone, as illustrated in Fig. 1B. The counter part of the depth of field in image space is called depth of focus, $\delta z'$.

2.3 Wiener skewing

A refractive gradient, characteristic of solutes redistributed within a sample cell during AUC experiments, alters the trajectory of rays passing through the solution column; see illustration in Fig. 1B. This phenomenon is related to the artifact dubbed Wiener Skewing appearing in AUC data with samples

of high concentration and high refractive increment.[18] The bending of rays through steep sedimentation boundaries will result in a skewing of the recorded solute distributions. Mathematical descriptions of Wiener Skewing were explored in regards to the early AUC refractometric optical systems and it was determined that imaging a plane 2/3 through the solution column, minimized the effects.[18,21] More recently, it was shown experimentally that at moderate concentrations, the effects have no appreciable impact on the results with the absorbance optics of the XL-A centrifuge.[22] However, at high concentrations, the refractive gradients may be so high that the rays are partly or even completely bent out of the aperture of the optics. The result may be recognized by the appearance of a so called 'black band' in absorbance data,[22] similar to a Schlieren optical peak, if the light is just partly deviated out of the aperture and the refractive index gradient is then recorded as apparent light absorption.[23] The 'black band' is of course a direct consequence of the NA of the optics. By imaging with a larger NA, the acceptance angle of emitted rays is likewise increased. In the case of diffraction-limited imaging performance, increasing the NA will in principle increase the resolving power of the lens, according to eqn (3). However, a larger NA also generally requires a shorter working distance, *i.e.* the distance from the lens to the object plane, and therefore is limited by the clearance of the optics and the centrifuge rotor. Furthermore, increasing the NA will decrease the diffraction-limited depth of field according to the inverse square, eqn (4).

Under consideration of Wiener skewing, the dependence of the resolution limit and the depth of field, a compromise is needed to specify the new optical system's numerical aperture. In order to limit the problem of black bands compared to the commercial XL-A system while keeping the depth of field as large as possible, we specify the numerical aperture with an acceptance angle, $\theta = 1.5°$. This is equal to the maximum acceptance angle of the XL-A imaging optics. This correspondingly defines the NA = 0.0262 and allows calculation of the resolution limit and diffraction-limited depth of field by eqn (3) and (4).

2.4 Error budget analysis

In this subsection several optical effects and potential errors that affect the radial resolution in AUC absorbance detection are discussed. In view of the previously specified numerical aperture, an error budget is established to estimate how much inevitable resolution loss is given, without considering the losses due to potential optical aberrations. With this procedure, we want to quantify the radial resolution limit in AUC absorbance detection. To consider the spectral range used in MWL devices, the analysis is performed at wavelength of 230, 465 and 700 nm.

2.5 Diffraction and effective point spread function

Solute absorption will take place across the entire 12 mm of solution column, and therefore an imaging system is concerned with capturing not only the detail of the ideal image plane, but also of the defocused regions above and below. If the defocused distance exceeds the optical system's depth of field, the resolution of the object details from these regions is worsened. The situation is depicted in Fig. 2 by the example of the PSF occurring from an event in focus and from defocused object planes within the solute. Because the detector measures the intensity not only from the object plane in focus but also from the defocused regions, the intensity distribution of an effective PSF on the image plane should be considered.

Because it is not clearly determined at which position within the solute a photon gets absorbed, the effective radial

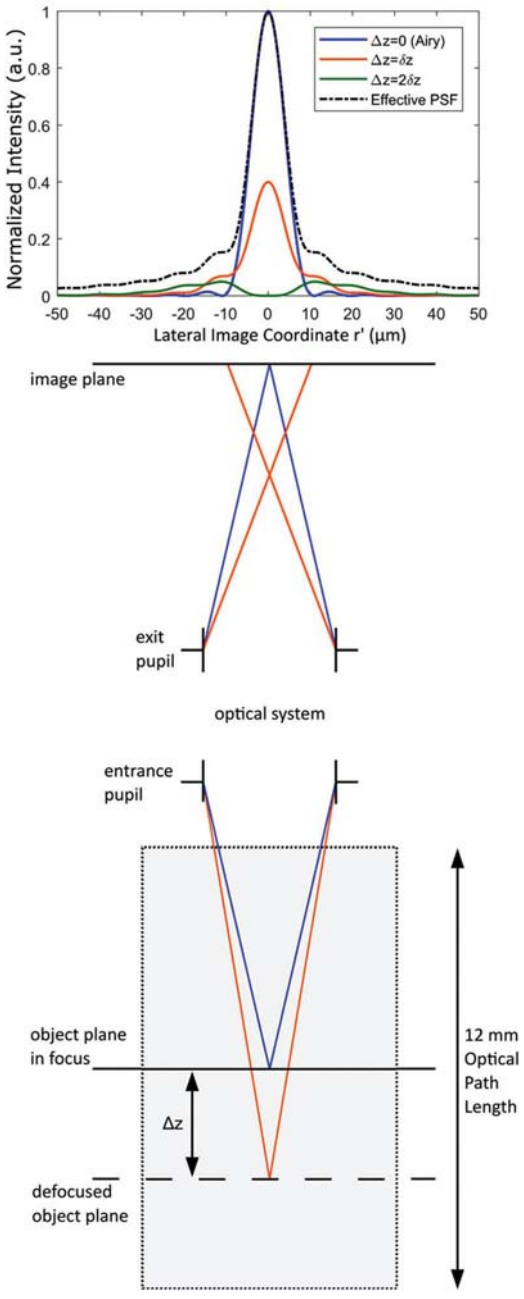

Fig. 2 Illustration of PSF defocus through an AUC sample solution column, for a defocus distance of Δz = 0 (blue line), δz (orange line), 2δz (green line), and by calculation of an integral effective PSF, modelled for 465 nm (dotted black line). Note; ray tracing not drawn to scale.

resolution is determined by overlap of defocused PSFs. Computational methods, and the basic principles from Fourier optics, were used to determine the lateral intensity distribution of an effective PSF. The effective PSF, we define as the integral over all perfect point spread functions through a defocus of the object plane within an interval of $-6\ \text{mm} < \Delta z < 6\ \text{mm}$, eqn (5);

$$I_{\text{eff}} = \int_{-6\,\text{mm}}^{+6\,\text{mm}} I_{\text{PSF}}(r', \Delta z)\,\text{d}(\Delta z) \tag{5}$$

Here r' is the lateral image coordinate, Δz distance between the defocused object plane and the object plane in focus, and I_{PSF} the lateral intensity distribution of the corresponding point spread function. Because only a defocus error and no aberrations are considered, the I_{PSF} (r', $\Delta z = 0$) corresponds to the Airy diffraction pattern. The calculations were performed with a numerical aperture of $\text{NA}_{\text{Obj}} = 0.0262$ and a paraxial magnification, of a magnitude, $|M| = 1$. For simplicity, sample specific refractive properties were not considered, *i.e.* $n = 1$ in object space.

The resulting effective point spread function for an example wavelength of 465 nm is illustrated in Fig. 2, along with the corresponding lateral intensity distribution of the Airy diffraction pattern. The result shows the effective point spread function is not significantly broadened compared to the Airy pattern. The intensity contributions from the out of focus planes slightly increase the outer ring region. Thus, the diffraction resolution limit seems still to be well approximated by the Airy radius. Therefore, the effect of diffraction sets the limit in radial resolution of $\Delta r_{\text{Diff}} = r_{\text{Airy}}$ for the shortest, longest and mid wavelengths as summarized in Table 1.

The detection optics of the different AUC platforms perform imaging onto a finite slit (12.7 μm wide for the XL-A and 25 μm for the MWL). Because the slit acts as a field stop on the image plane, most intensity from strong defocused events is blocked. The depth of field is very small compared to the 12 mm optical path length of the sample cell, and therefore the recorded intensity signal comes from only a thin region around the object plane in focus. Intensity contributions from defocused object planes which significantly extend across the slit dimension are blocked and details within this region are not captured in the measurements. As an example, the lateral point spread functions for a defocus distance of δz and $2\delta z$ are additionally illustrated in Fig. 2.

Table 1 Diffraction limited and final radial resolution and diffraction-limited depth of field estimates for wavelengths at the ends and middle of the spectral range

λ (nm)	Δr_{Diff} (μm)	δz (mm)	Δr_{Final} (μm)
230	5.35	0.34	5.89
465	10.83	0.68	11.10
700	16.30	1.02	16.48

2.6 Additional error contributions

Additional features of AUC optical imaging that have not, to our knowledge, been fully explored include the effects of rotor precession and the limitation due to the arc of isoconcentration. For AUC rotors to be balanced, cells in opposing sides of the rotor are limited to a weight difference of no more than 0.5 grams. Nevertheless, misbalances of less than 0.5 grams across the rotating diameter, may in principle lead to precession of the rotor, *i.e.* a wobbling of the rotational axis about the center of mass. Because the periodic modes of precession will often be asynchronous with the rotor, it is presumed that any significant amount of precession would be apparent in the experimental data, particularly for sharp noise artifacts like a window scratch. Because this is not observed in practice, it is assumed that any effects of precession are very small; less than $\Delta r_{\text{Rotor}} = 1$ μm.

The centrifugal field applied by the spinning rotor will act outward, radially from the center axis of rotation. The sedimentation process will subsequently follow the trajectory of the centrifugal field, producing differential arcs of isoconcentration. Because scanning absorbance detectors typically utilize a linear slit mask for 1-dimensional imaging, the concentration increment measurements will always have a slightly biased gradient due to the isoconcentration arc. It is estimated from the cell channel geometry that this error is limited to below $\Delta r_{\text{Arc}} = 2$ μm from top to bottom.

The scanning mechanism can also have an error contribution. This may take the form of a systematic offset, as was realized by Ghirlando *et al.*, or could appear as random 'jitter'.[24] Even though the origin is mechanical, the resulting data artifact will be indistinguishable from optical effects. With modern stepper motor devices, the scanning precision is below $\Delta r_{\text{Scan}} = 1$ μm.[25]

2.7 Final error budget

According to the previous analysis, the final error budget is given by eqn (6);

$$\Delta r_{\text{Final}} = \sqrt{\Delta r_{\text{Diff}}{}^2 + \Delta r_{\text{Rotor}}{}^2 + \Delta r_{\text{Arc}}{}^2 + \Delta r_{\text{Scan}}{}^2} \tag{6}$$

The results for wavelengths 230, 465 and 700 nm are listed in Table 1. This calculated loss in radial resolution sets an inevitable limit for the specified numerical aperture. The analysis shows, that diffraction contributes the most to the error budget. Any potential additional contribution, such as optical aberrations or manufacturing and alignment errors of the optical components will worsen the radial resolution of the imaging optics.

3. Results & discussion

3.1 XL-A optics

The XL-A absorbance optical system was first introduced in 1991, and the basic architecture of the original design is described in ref. 4. The XL-A imaging optics consist of a so-

called slit-lens assembly. Two plano convex lenses focus the mid-plane of a sample cell onto a slit (12.7 μm in the y dimension and 1 mm in x dimension) in a thin mask above a photomultiplier tube, see Fig. 3. A. Note; 12.7 μm is the physical dimension of the slit, with $M = -0.6$ the optically effective size is 25 μm. This is analogous to an effective pixel size. This was confirmed by reticle calibrated microscopy (data not show).

The lens and slit are scanned by a servo motor across the face of the photomultiplier tube to record radial increments.

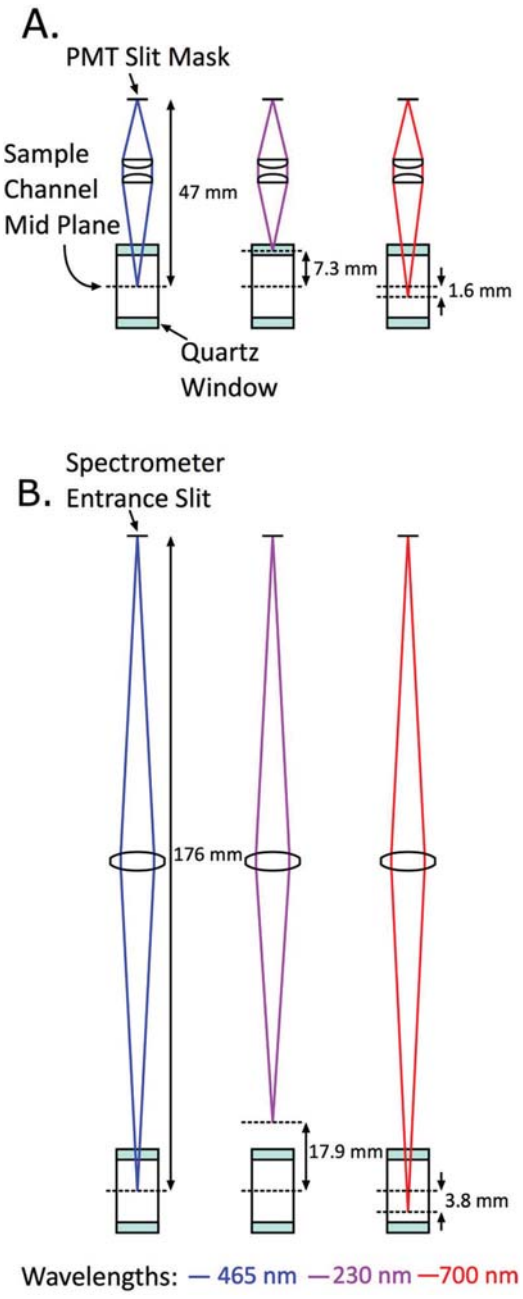

Fig. 3 Illustration of the basic optical imaging arrangement for the XL-A optics (A.), and the MWL optics (B.). Right; Illustration of the wavelength dependent focus shift for the XL-A optics and the MWL optics for 230 nm (purple) and 700 nm (red).

However, a complete description of the design parameters is not provided anywhere, and no information is given about the basic imaging properties.

Using the simple description available for the optics,[4] basic measurements that could be gathered with a machinists caliper and a few reasonable assumptions, it is possible to reverse engineer the remaining parameters that define the XL-A imaging optics. By disassembling some of the optical system, the total track length was measured from the object (midplane position of a sample cell), to the image plane (slit above the photomultiplier tube), as well as the thickness and distance between the two imaging lenses. The dimensions were entered into *OpticStudio*, along with the safe assumption that the lenses are made of fused silica, having refractive properties identical to quartz. Additionally, the XL-A does not use a circular aperture, but for simplification can be modeled by a circular dimension matching the 1 mm aperture diameter along the radial coordinates directly above the first lens. We also made the assumption that the curvatures of both lenses are the same.

In order to determine a reasonable value for the unknown radius of curvature, a default Merit Function was created in *OpticStudio* to perform an optimization on the minimum RMS spot radius of the on-axis field point. To consider the geometrical measurements, design constraints were enforced by using the *Solves* function in *OpticStudio*.[16]

A local optimization was performed at a wavelength of 588 nm; a typical wavelength for tabulated lens data. The result is a lens radius equal to 9.735 mm and an effective focal length of 21.23 mm. Because manufactured lenses are typically produced with sensible focal length increments, for example 15, 20 or 25 mm, we assume the true effective focal length to be 20 mm. This implies a lens radius of 9.17 mm.

Spot diagrams in *OpticStudio* are used to evaluate the imaging performance of the reverse engineered XL-A optics. We choose for our initial investigations a wavelength of $\lambda = 465$ nm, which is the mid-wavelength within the spectrum used in multi-wavelength detection. Because the lens-slit assembly is adjustable for focusing, we optimized the position of the lens unit within the track length to achieve a minimal RMS spot radius of the on-axis field point. In this configuration the system has a paraxial magnification of approximately $M = -0.6$. Because of this, we applied another object field point at an off-axis distance of 1 mm to ensure consideration of the maximum off-axis distance, which is reaching the 12.7 μm wide and 1 mm long slit mask above the photomultiplier tube.

In this configuration, the polychromatic imaging performance was evaluated by applying 230 and 700 nm as additional wavelengths. The spot diagrams in Fig. 4A, clearly show that the shortest and longest wavelength are extremely defocused. In comparison, the spots for 465 nm, for which the lens positions were optimized, are so small they are not visible in the same spot diagram. A comparison of the RMS spot radius and the Airy radius for the whole wavelength range is given by Fig. 4B. This graph shows clearly that diffraction-limited imaging performance is not possible for the whole wavelength

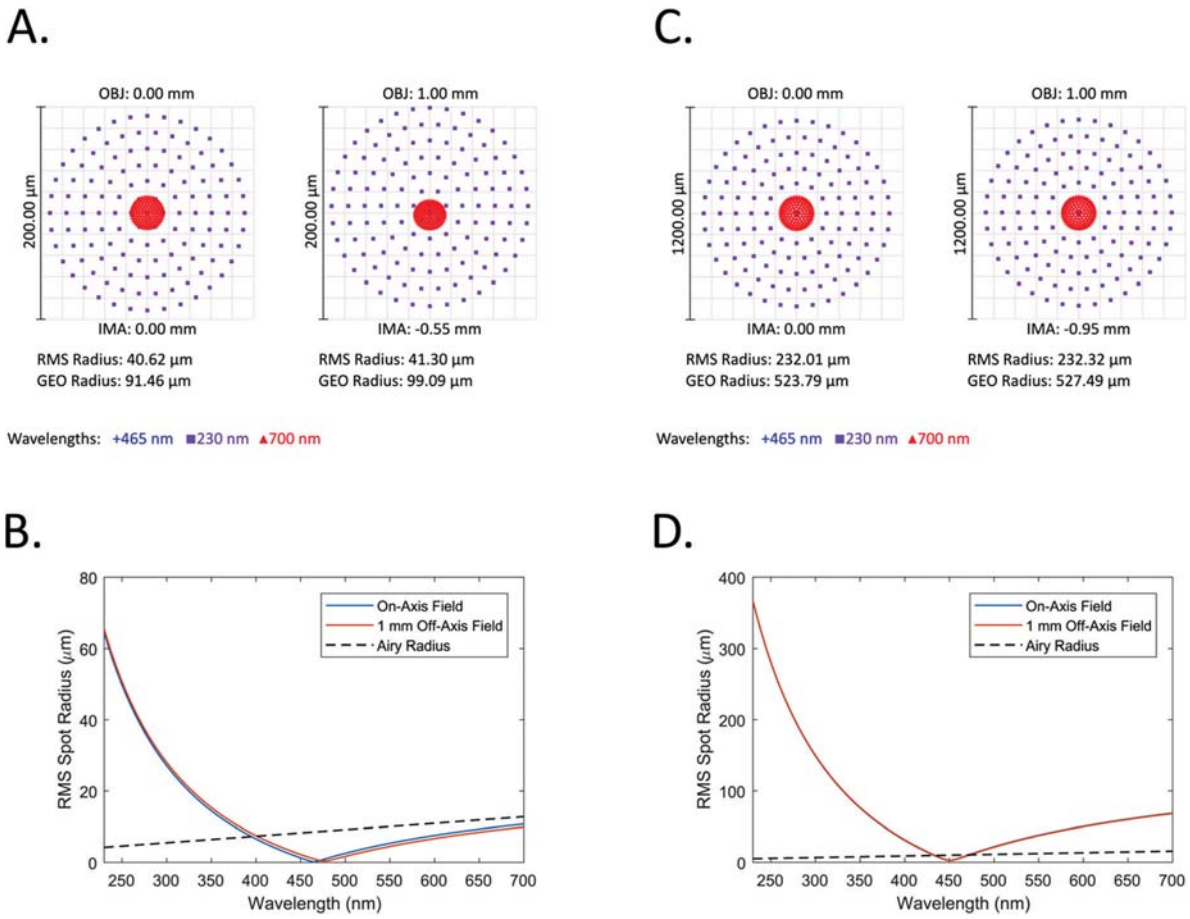

Fig. 4 Spot diagrams modelled by OpticStudio, for an on-axis object field point and 1 mm off-axis object field point, for three wavelengths, for the XL-A optics (A.), and MWL optics (C.). RMS and GEO values are for the polychromatic bandwidth spanning 230 to 700 nm. Corresponding plots of RMS spot radius *versus* wavelength for the XL-A optics (B.), and MWL optics (D.).

range. Due to the strong wavelength dependency of the refractive index of quartz in the UV, the shortest wavelengths exhibit the largest amount of axial chromatic aberration. The effect of axial chromatic aberration can also be interpreted as the optical system focusing light from different distances in object space. To determine which planes in object space are in focus for which wavelength, the object plane positions were optimized in the *OpticStudio* model for the shortest and longest wavelength. The investigations show that the wavelength of 230 nm is focused on a plane 7.3 mm above the cell's mid-plane while the wavelength of 700 nm on a plane 1.6 mm below. The situation is illustrated in Fig. 3A.

While the XL-A optics are clearly shown to be inadequate for broadband imaging, the possibility for diffraction limited imaging over a narrow wavelength band is reassuring for users of the instrument that confine their measurements to limited spectral domains. For example, the large body of work with biopolymers that only absorb in the UV can be within reasonable error tolerances when focused on the proper plane. However, to our knowledge, the XL-A imaging optics are rarely adjusted for focus during routine servicing. Defocused imaging, as manifest in distorted sedimentation boundary shapes, is a likely contributor to the precision of the XL-A instruments, as noted in ref. 26, but has not been explored in any publication relating to the instrument performance.

It is important to note, that if there is a small discrepancy in one of the assumptions leading to a change in one of the estimated parameters, it does not have a meaningful influence on the overall conclusions presented. The calculated optical parameters were additionally verified by experimental testing (results not shown)‡.

3.2 Multiwavelength lens optics

The MWL detection optics were first introduced in 2006,[8] and have been described previously,[10,11] but never evaluated for optical parameters. The optics consists of a simple bi-convex quartz lens from *Linos* (Model: G0633118000), focusing onto the 25 µm entrance slit of a spectrometer. The focal length of

‡The new Optima AUC recently released from Beckman appears to use nearly identical imaging optics to those of the XL-A with upgrades only to the scanning mechanics. Therefore the results presented here may also apply to the newest commercial instrument, with the important caveat of the illumination effects discussed in the Conclusion.

the lens, at the *Linos* catalog design wavelength of 248 nm is 40 mm, and an adjustable iris determines the clear aperture. In practice, the iris is opened until the detector records a reasonable intensity signal. Depending on the sample, the diameter of the iris is between 2 and 5 mm.

The position of the lens within the track was chosen similar to match the position used in practice and a primary wavelength of 465 nm was applied again. To make the setup comparable in refractive gradient limitations to the XL-A detection optics, we set the aperture diameter of the iris in the *OpticStudio* model to 4.5 mm which corresponds to the maximum acceptance angle of 1.5° of the XL-A detection optics. We apply again 230 and 700 nm as additional wavelengths for investigation. The paraxial magnification of this setup is approximately $M = -1$ and, therefore we choose again an additional off-axis object field point at a distance of 1 mm, to illustrate a distance beyond what is required.

The spot diagrams in Fig. 4C show that this system suffers from strong axial chromatic aberration. The defocus for the shortest and longest wavelength is greater than for the XL-A system. A plot of the RMS spot radius *versus* the wavelength shows, at a narrow bandwidth around 450 nm, the RMS spot radius is slightly smaller than the Airy radius, Fig. 4D. This indicates that the system is in focus only for this small range of wavelengths.

Because the RMS spot radius is, for most of the wavelengths, larger than the radial dimension of the spectrometer slit, the system has suboptimal performance in imaging the cell's mid-plane and is far from an ideal solution for broadband operations.

Similar to the evaluation of the XL-A optics, it was examined how focus shift in object space behaves. The object plane position was optimized for minimizing the RMS spot radius for 230 and 700 nm. The results, illustrated in Fig. 3, show how significant the inherent chromatic aberration of this system is. In the case of the mid-wavelength alignment, where the optical system is focusing on the mid-plane, the best object plane for 700 nm is located 3.8 mm behind the mid plane and for 230 nm the optics focus on a region about 17.9 mm in front of the mid-plane – completely out of the cell.

The main problem of this system, as with the XL-A optics, is axial chromatic aberration. In fact, it's obvious that a single element lens is insufficient for broadband operations capturing the UV and visible spectrum.

It is important to note that due to the beam geometry provided by the illumination optics, the power density of the image formation by the optics will not be uniform. Instead, the light rays that are near to coincident with the optical axis will dominate the image field. The rays closest to paraxial will of course experience less refractive power through the lenses and subsequently less chromatic aberration. This likely explains how the MWL optics are able to perform better in practice, than anticipated by the models previously described.[5]

3.3 Mirror optics design

A common method to reduce chromatic aberration is the use of achromatic lens optics made of at least two materials with different dispersion properties. In this case the extra challenge in broadband AUC operations is the requirement of transmission in the deep UV. This requires achromatic lens systems for UV applications made of CaF_2 and fused silica. The modeling of the beam path with such achromatic stock optics showed, that the remaining chromatic focal shift across the desired spectral range is not sufficient for broadband AUC applications. In order to overcome the problem of chromatic aberration, a new optical system based on off-axis parabolic mirrors (OAPMs) was designed. A pair of OAPMs is able to perform diffraction-limited on-axis imaging, if the on-axis object field point is located at the focal point of one of the mirrors. Investigations with optical design modeling in Brückner *et al.* showed that the arrangement where the axes of the parent parabolas are coincident (see Fig. 5A) produces the smallest amount of geometrical aberration but suffers from large distortion compared to other geometric arrangements.[27] Because distortion increases cubically with the field height (see eqn (1)), it is not problematic for scanning optics, because we cover only a very small field of view. However, such an arrangement cannot be realized because of spatial limitations within the vacuum chamber of the AUC.

The best mounting possibility on the scanning arm is offered by the arrangement where the parabolas are rotated 180° about their common axis with an additional flat mirror, as shown in Fig. 5B. An adjustable iris may be integrated in between the OAPMs to attain the desired acceptance angle of 1.5°. This offers the possibility to enlarge the aperture in experiments with samples of strong refractive index gradients to avoid the manifestation of black bands. One problem of this OAPM arrangement is that astigmatism of both OAPMs adds up and enlarges the geometrical spot of confusion.[27] However, the evaluation of the RMS spot radius will show that this effect is not an issue for the small field of view in AUC absorbance detection.

For the new mirror design, stock dimension 90° OAPMs were selected from the *Thorlabs* catalog with reflective focal

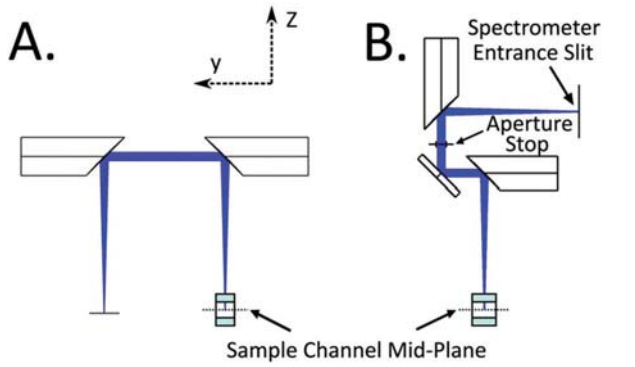

Fig. 5 (A.) Cross-section illustration in the z–y object plane of off-axis parabolic mirrors arranged where the axis of the parent parabolas are coincident. (B.) Adaptation of a plane 90° mirror between the off-axis parabolic mirrors, such that the optical system can fit within the centrifuge vacuum chamber, while minimizing the geometric spot of confusion.

lengths of 101.6 mm, to fit within the mechanical constraints of the scanning arm. For investigating the optical performance of the new design, the parameters of the two OAPMs and the plane mirror were implemented in *OpticStudio* and arranged in the same way as to be mechanically constructed on the detector arm. Additionally, the simulation model includes the quartz window of the measurement cell and the aperture is located in between the OAPMs. To achieve the maximum acceptance angle of 1.5°, the diameter of the aperture was scaled to 2.6 mm. The cross section of the simulation model as well as the coordinate system of the object plane is illustrated in Fig. 5B. The positive *y*-axis is oriented left, the z axis is aligned along the optical axis and the positive *x* axis is into the plane of the drawing.

As object field points we choose for evaluation (x, y) = (0 mm, 0 mm), (0 mm, 1 mm), (0 mm, −1 mm) and (1 mm, 0 mm) to respect the asymmetry of the OAPMs. A consideration of the off-axis distance in the negative x-direction is not needed because the curvature of the OAPMs in this direction is symmetrical. Because both OAPMs have the same reflective focal length, the paraxial magnification of the system is $M = -1$. The maximum off-axis distance of the modeled object field points is much greater than the dimensions of the spectrometer slit, to illustrate the aberration effects in the spot diagram. However, it is also prudent to consider a larger off-axis distance in the event of misalignments of the spectrometer.

The only refractive element in the simulation model is the quartz window of the cell. This induces a small chromatic focal shift of 133 μm. The position of the image plane, *i.e.* the location of the spectrometer slit, was optimized for λ = 300 nm; the wavelength corresponding to the middle of the chromatic focal shift range. Therefore, the spot diagrams are evaluated at λ = 300, 230 and 700 nm in Fig. 6A. The spot diagram of the on-axis field shows the small amount of axial chromatic aberration induced by the quartz window. In the case of the off-axis field points, additional contributions of astigmatism and lateral chromatic aberration are recognizable. Compared to the Airy disk of the primary wavelength of 300 nm, the geometrical spot of confusion of all three wavelengths is definitely smaller. Fig. 6B shows that the RMS radius for all wavelengths is below the corresponding Airy radius, meaning that the system performs polychromatic diffraction-limited imaging.

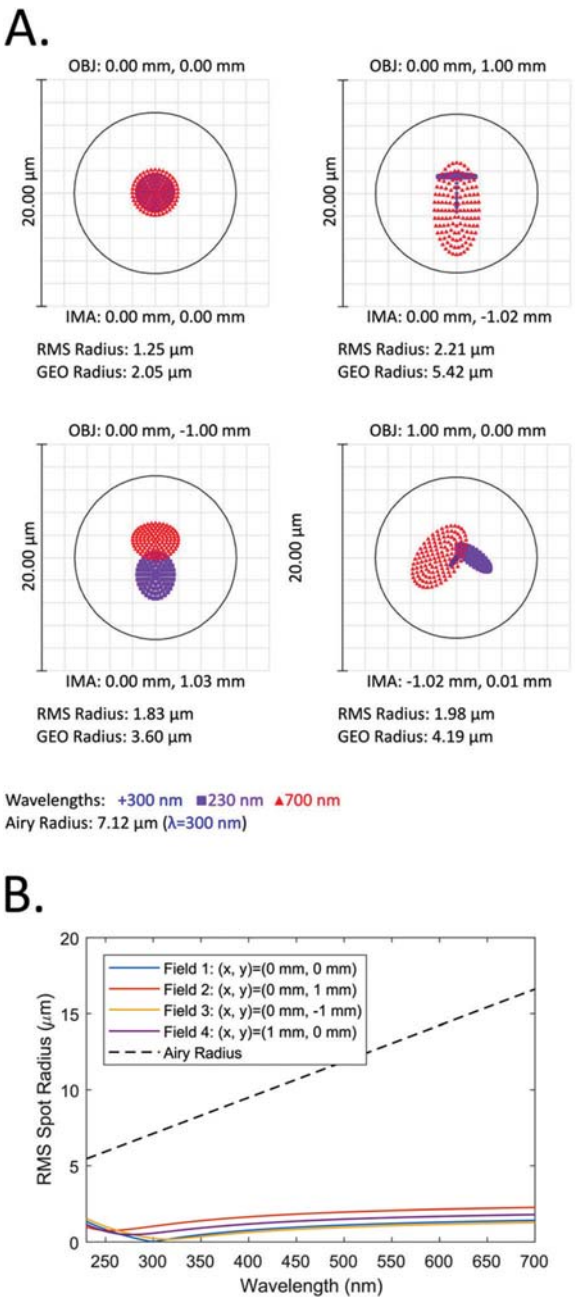

Fig. 6 (A.) Spot diagrams modelled by OpticStudio, for an on-axis object field point and a 1 mm off-axis distance in different directions to respect the mirror systems' asymmetry, for three wavelengths, for the mirror imaging optics. RMS and GEO values are for the polychromatic bandwidth spanning 230 to 700 nm. (B.) Corresponding plots of RMS spot radius *versus* wavelength for mirror imaging optics.

4. Conclusions

New AUC instruments are presently being developed commercially and in academia. With the arrival of improved instrumentation, data quality will become an increasingly important consideration, and come under scrutiny in debates over pushing the limits of measurement capabilities. Whether it is probing the dynamic range of the optics with highly concentrated solutions, pushing the limit of detection for trace quantities or attempting to estimate the fundamental parameters of an interacting system, detection performance will continue to be at the forefront of method advancement. The advanced analytical methods now commonplace in AUC data evaluation will operate in tandem with instrument performance to expand the possibilities of AUC in scientific investigations. Modern AUC data evaluation techniques routinely apply corrections for systematic noise sources. For example time invar-

iant noise, radially invariant noise and time stamp corrections. However, optical aberrations add additional systematic data that has never before been completely characterized or corrected for. Analytical methods in programs such as UltraScan are continually being developed for MWL data and feature tools to at least partially correct for spectrally correlated noise.[28]

A subsequent investigation should consider how optical aberrations could influence results. For instance, defocus will produce a broader intensity distribution of the point image and will appear to broaden the sedimentation boundary. The shape of the sedimentation boundary in turn has significant implications on the modeling of diffusion or polydispersity. While previous publications[26] have suggested the possibility of optical effects creating discrepancies appearing in evaluations, this is the first publication of its kind that seeks to quantitatively identify the possible origins of such optical effects. And, to also show which contributions are likely or unlikely to be significant. Chromatic aberration was shown to be the most significant contributor to resolution in the lens-based system. This was also highlighted recently in experimental demonstrations.[5] New lens-based designs, with spectral scanning architecture, may consider a re-focusing mechanism to circumvent the chromatic aberration limitations.

The preceding results introduce a framework for application of modern optical modeling techniques to AUC absorbance detectors. We show rigorous evaluation of the imaging capabilities for the existing commercial XL-A, and the open source MWL instrument. In both cases we demonstrate the optics are severely limited by chromatic aberration for broadband detection. To overcome these limitations a new mirror based optical system is proposed. This design was the inspiration for a broadband detector system recently implemented.[5] The experimental results in Pearson *et al.* showed that the broadband imaging performance was strongly dependent on the illumination optics. A prototype with mirror focused illumination and mirror imaging was shown to have the best results.

The reported dependency of illumination optics on the imaging performance is a likely explanation of how the AUC optics are able to perform better in practice, than anticipated by the models described herein. Because light rays nearest to coincident with the optical axis have minimal optical transformation, but possess the highest power density and dominate image formation. The illumination dependency also points to the obvious path forward for a future design strategy. Continuation of this work should consider the effects of illumination beam design by extending the model to include power throughput predictions. However, such an approach is mathematically more challenging, and beyond the scope of this manuscript. A model that includes beam shaping may also include the effects of sample gradient refraction, to avoid 'black band' formation and minimize Wiener skewing. Such a study should consider a light-sheet confocal design that under-fills the NA of the imaging optics. This approach could also be used to optimize for both imaging resolution and signal-to-noise ratio, which are often inversely correlated.[5] Furthermore, these principles may also apply to other free boundary solution instruments such as membrane-confined electrophoresis.[29]

Conflicts of interest

There are no conflicts to declare.

Acknowledgements

J. P. and H. C. acknowledge financial support by the Center for Applied Photonics (CAP) at the University of Konstanz.

Notes and references

1 J. L. Cole, J. W. Lary, T. P. Moody and T. M. Laue, *Methods Cell Biol.*, 2008, **84**, 143–179.
2 W. Maechtle and L. Börger, *Analytical ultracentrifugation of polymers and nanoparticles*, Springer, Berlin, New York, 2006.
3 G. Ralston, *Introduction to Analytical Ultracentrifugation*, Beckman Instruments, Fullerton, CA, 1993.
4 S. E. Harding and J. C. Horton, *Analytical ultracentrifugation in biochemistry and polymer science*, Royal Society of Chemistry, 1992.
5 J. Pearson, J. Walter, W. Peukert and H. Cölfen, *Anal. Chem.*, 2017, **90**, 1280–1291.
6 H. M. Strauss, E. Karabudak, S. Bhattacharyya, A. Kretzschmar, W. Wohlleben and H. Cölfen, *Colloid Polym. Sci.*, 2008, **286**, 121–128.
7 T. Laue, *Choosing Which Optical System of the OptimaTM XL-I Analytical Ultracentrifuge to Use*, Beckman Instruments, Fullerton, CA, 1996.
8 S. K. Bhattacharyya, P. Maciejewska, L. Börger, M. Stadler, A. M. Gülsün, H. B. Cicek and H. Cölfen, in *Analytical Ultracentrifugation, Progress in Polymer and Colloid Science*, Springer, Berlin Heidelberg, 2006, vol. VIII, pp. 9–22.
9 H. Cölfen, T. M. Laue, W. Wohlleben, K. Schilling, E. Karabudak, B. W. Langhorst, E. Brookes, B. Dubbs, D. Zollars, M. Rocco and B. Demeler, *Eur. Biophys. J.*, 2010, **39**, 347–359.
10 E. Karabudak and H. Cölfen, in *Analytical Ultracentrifugation; Instrumentation, Software and Applications*, Springer, 2016, pp. 63–80.
11 J. Pearson, F. Krause, D. Haffke, D. Demeler, K. Schilling and H. Cölfen, *Methods Enzymol.*, 2015, **562**, 1–26.
12 J. Walter, D. Segets and W. Peukert, *Part. Part. Syst. Charact.*, 2016, **33**, 184–189.
13 H. Zügge, H. Gross, M. Peschka and F. Blechinger, *Handbook of Optical Systems, Volume 3: Aberration Theory and Correction of Optical Systems*, John Wiley & Sons, 2007.

14 H. Gross, *Handbook of Optical Systems: Volume 1: Fundamentals of Technical Optics*, John Wiley & Sons, 2005.
15 R. E. Fischer, B. Tadic-Galeb, P. R. Yoder, R. Galeb, B. C. Kress, S. C. McClain, T. Baur, R. Plympton, B. Wiederhold and A. J. Grant, *Optical system design*, Citeseer, 2000.
16 OpticStudio User Manual, Zemax, 2015.
17 P. Lloyd, *Optical Methods in Ultracentrifugation, Electrophoresis and Diffusion*, Oxford University Press, Great Britain, 1974.
18 H. Svensson, *Opt. Acta*, 1954, **1**, 25–32.
19 J. J. Correia and W. F. Stafford, in *Methods in enzymology*, Elsevier, 2015, vol. 562, pp. 49–80.
20 J. Pawley, *Handbook of biological confocal microscopy*, 1990.
21 H. Svensson, *J. Mod. Opt.*, 1956, **3**, 164–183.
22 J. M. González, G. Rivas and A. P. Minton, *Anal. Biochem.*, 2003, **313**, 133–136.
23 H. Cölfen, P. Husbands and S. Harding, in *Analytical Ultracentrifugation, Progress in Colloid & Polymer Science*, Springer, 1995, pp. 193–198.
24 R. Ghirlando, A. Balbo, G. Piszczek, P. H. Brown, M. S. Lewis, C. A. Brautigam, P. Schuck and H. Zhao, *Anal. Biochem.*, 2013, **440**, 81–95.
25 Z. T. Inc., T-LA28A: Miniature linear actuator, https://www.zaber.com/products/product_detail.php?detail=T-LA28A&tab=Series Features.
26 H. Zhao, R. Ghirlando, C. Alfonso, F. Arisaka, I. Attali, D. L. Bain, M. M. Bakhtina, D. F. Becker, G. J. Bedwell and A. Bekdemir, *PLoS One*, 2015, **10**, e0126420.
27 C. Brückner, G. Notni and A. Tünnermann, *Optik*, 2010, **121**, 113–119.
28 C. N. Johnson, G. E. Gorbet, H. Ramsower, J. Urquidi, L. Brancaleon and B. Demeler, *Eur. Biophys. J.*, 2018, 1–9.
29 T. M. Laue, A. L. Hazard, T. M. Ridgeway and D. A. Yphantis, *Anal. Biochem.*, 1989, **182**, 377–382.